

Simulation of Solid-State Sensors for a Spark Chamber Trigger System

Part III Project Report

Supervisor: Dr. Steve Wotton

BGN: 8234S

May 2021

ABSTRACT:

Photomultiplier tubes (PMTs) are currently employed as part of a trigger system for a spark chamber held at the Cavendish Laboratory. Advances in solid-state sensor technology have presented silicon photomultipliers (SiPMs) as a potential alternative to these traditional PMTs. In this project, we use circuit simulation software to simulate a SiPM using an equivalent circuit model. The results from the simulations are found to be consistent with theory.

In order to assess the feasibility of these devices in a trigger system, it is crucial to understand how a SiPM operates and its important features. Having a working model is very useful in this aspect and in future work, can be complementary to experimental measurements obtained from working with SiPMs.

Except where specific reference is made to the work of others, this work is original and has not been already submitted either wholly or in part to satisfy any degree requirement at this or any other university.

1 INTRODUCTION

A spark chamber is a particle detector originally used as a research tool from the 1930s onwards and was a precursor to more sophisticated detectors such as bubble chambers in the 1960s. Nowadays, spark chambers are mostly found in museums or used as educational tools to promote particle physics and physics in general. [1]



Fig. 1.1: Taken from [1]. The spark chamber built and used by the Cambridge HEP group.

The High Energy Physics (HEP) group at Cambridge University has its own spark chamber for educational and promotional purposes (Fig. 1.1). By taking advantage of recent advances in solid-state photon sensor technology, it is believed that the photomultiplier tubes (PMTs) currently in use in the trigger system can be replaced in favour of these solid-state sensors. These devices have a number of advantages over traditional PMTs, most notably: a higher quantum efficiency¹,

an insensitivity to magnetic fields and a more compact design. [2]

Silicon photomultipliers (SiPMs) are becoming increasingly well established in various fields of physics. For example, the SiPM's capability to detect single photons and its excellent timing resolution (in the 200ps range) has made their use ideal in time-of-flight PET (TOF-PET). Their insensitivity to magnetic fields has also naturally led to their implementation in MR-based systems where PMTs were previously unsuitable. [3] In HEP, one of the earliest large scale adopters of SiPMs was in the T2K neutrino oscillation experiment. 60,000 SiPMs were used - each made up of a customised $1.3 \times 1.3\text{mm}^2$ pixel with a $50\mu\text{m}$ microcell pitch. [4]

By utilising an analog circuit simulator, a SiPM is simulated using an equivalent circuit model. These simulations will help in understanding how a SiPM operates, which is crucial in assessing their suitability in a spark chamber trigger system. The features of a SiPM will need to be known and their impact carefully considered.

2 THEORY

2.1 Overview

Spark chambers consist of a sealed chamber filled with a gas such as helium or neon and in which a stack of conducting metal plates is placed (Fig. 2.1). As cosmic rays pass through the device, scintillators at the top and bottom of the chamber form the basis of a trigger system that applies a high voltage be-

¹Quantum efficiency is a measure of a photode-

vice's effectiveness in converting incident photons into electrons. It indicates how much current is produced when photons of a given wavelength is absorbed.

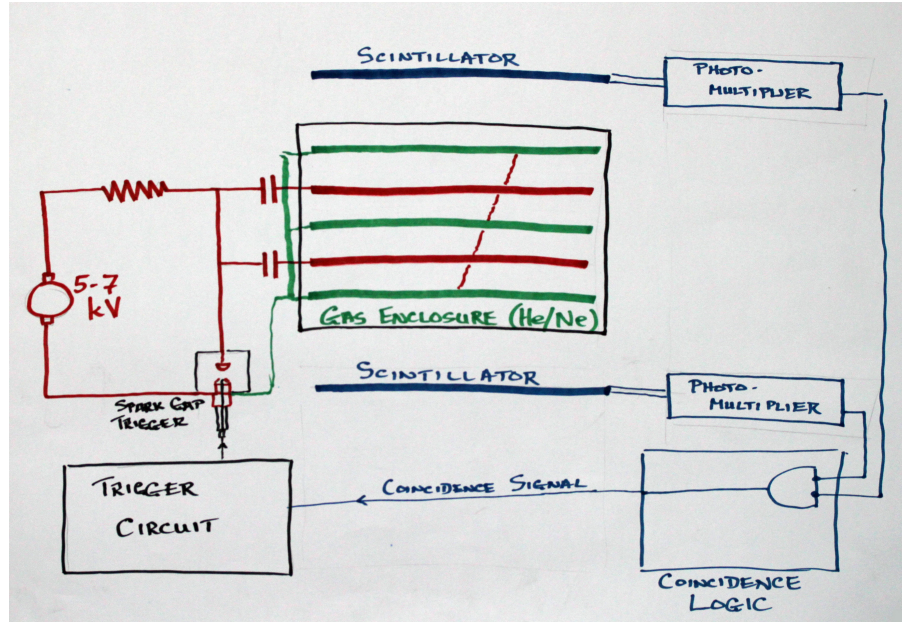


Fig. 2.1: Taken from [1]. Schematic diagram of the spark chamber.

tween each adjacent pair of conducting plates every time a cosmic ray is detected. The ionising particles in the cosmic rays ionise the gas inside the chamber and when a high voltage is applied, sparks form between the plates that follow the path of an ionising particle. Thus, the paths of the ionising particles can be observed within the spark chamber and recorded.

[1]

The scintillators, when excited by ionising radiation, spontaneously emits photons upon relaxation back into lower energy states. The photomultipliers absorbs these photons, converts it into an electric signal and amplifies the signal for use in the logic circuitry of the trigger system. The spark chamber currently uses traditional PMTs to achieve this; via the photoelectric effect, incident photons are converted into electrons that are then accelerated across a high voltage through intermediate stages (dynodes). [5]

PMTs have a number of advantages: high

eternal gain ($10^6 - 10^7$), low noise, fast response times and a good ability to resolve single photons. However, as previously mentioned, these devices also have low quantum efficiency, are susceptible to magnetic fields and are typically bulky and sensitive to handling. [2] SiPMs offer a potential improvement to such traditional PMTs.

2.2 SPADs

Single photon avalanche diodes (SPADs) can be considered to be the basic building blocks of SiPMs. As a photodetector, SPADs are based on p-n junctions that are specifically designed to operate above its breakdown voltage (V_{br}). [6] Usually, when the reverse bias voltage is low, the current is proportional to the number of incident photons.² However,

²This is the regime for avalanche photodiodes (APDs).

when the bias voltage is increased to above the cell's breakdown voltage, the electric field becomes so high that a single photon can trigger a self-sustaining avalanche via impact ionisation. This self-sustaining avalanche has to subsequently be quenched by lowering the voltage back down to V_{br} or below. The cell is then reset back to the bias voltage (V_{bias}), allowing another photon to be detected. [7] Fig 2.2 shows the process diagrammatically.

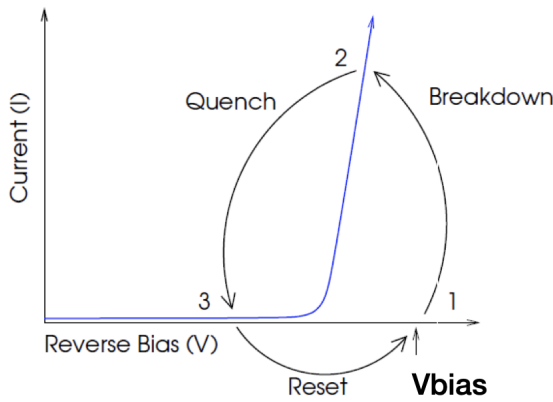


Fig. 2.2: Taken from [8]. When a SPAD is triggered by a photon, a current continues to flow until it is quenched back below the breakdown voltage. The SPAD is then reset back to the bias voltage.

An equivalent circuit for a SPAD is given in Fig. 2.3. The capacitor C_d is initially charged up to V_{bias} and no current flows through the device. When a photon is absorbed by the device, the switch is closed allowing C_d to discharge through R_d and consequently results in a voltage drop across R_q . As a result, a current flows through R_q characterised with a exponential rise time $\tau_d = R_d(C_d + C_q)$. Thus, the leading edge marks the photon arrival time and it can been shown that this leads to the best timing resolution. [9] Fig. 2.4 provides an example of the current through R_q ; the current reaching an asymptotic value:

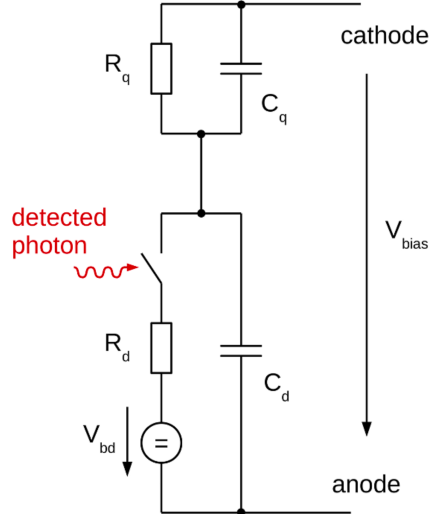


Fig. 2.3: Adapted from [3]. An equivalent circuit for a SPAD.

$$I_{max} = \frac{V_{ov}}{R_q + R_d} \approx \frac{V_{ov}}{R_q} \quad (2.1)$$

where we have $V_{ov} = V_{bias} - V_{br}$ and $R_q \gg R_d$. At this point, the system is quenched by R_q and the current exponentially falls back to a 'ready' state with recovery time: [10]

$$\tau_r = R_q(C_d + C_q) \quad (2.2)$$

It is a general rule that I_{max} should not exceed $20\mu A$. [11] Thus, for $V_{ov} = 1V$, the minimum value for R_q is around $50k\Omega$. At values below this, the circuit is not adequately quenched. The integrated quenching circuit in series with the SPAD is known as passive quenching; alternative methods of quenching are possible. [7]

The gain is defined to be the number of charge carriers produced per avalanche and one can calculate it by the integral of the current and dividing through by the elementary charge, $q = 1.602 \times 10^{-19}$. This is typically

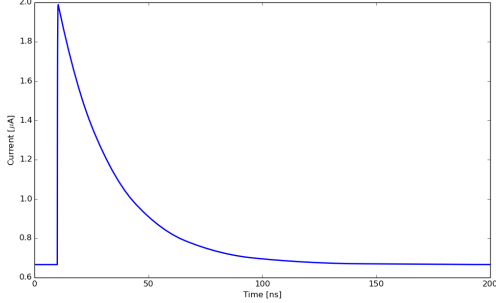


Fig. 2.4: The current of a simulated SPAD measured through R_q . With values of $R_q = 500k\Omega$, $R_d = 1k\Omega$, $C_d = 50fF$ and $C_q = 20fF$, there is an exponential rise time $\tau_d = 0.07ns$ and fall time $\tau_r = 35ns$.

in the order of $10^5 - 10^7$ - a gain comparable to PMTs. For a SPAD with a integrated quenching circuit, the gain is generally well-defined due to the uniformity of the internal capacitances: [3]

$$G = \frac{Q}{e} = \frac{(C_d + C_q)V_{ov}}{e} \quad (2.3)$$

One of the properties of a SPAD is that, when a photon is detected, the current remains flowing through its terminals unless the device is quenched. Thus, the SPAD acts as a binary device and its behaviour is independent of the number of photons impinging on the device³; we cannot differentiate between the arrival of single photons and many photons. This issue is resolved in the case of a SiPM by implementing many SPADs in parallel.

³This is why a SPAD is sometimes known as a Geiger-mode avalanche photodiode (GM-APD) in the literature.

2.3 SiPMs

2.3.1 Overview

SiPMs are formed by connecting many SPADs in parallel; for example, a $1\times 1mm^2$ SiPM with a $50\mu m$ microcell pitch contains 400 individual SPADs. Since the SPADs are connected in parallel, they are independent of each other and hence, when multiple photons impinge on the SiPM at the same time, an equivalent number of microcells are fired. Each microcell contributes to the output signal; if N photons are detected by N microcells, the output signal is N -times higher than that of a single photon. Thus, we are able to count the number of photons detected by the device. Fig. 2.5 shows a schematic diagram of a SiPM.

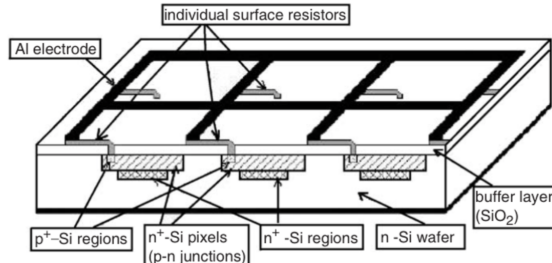


Fig. 2.5: Taken from [12]. Schematic diagram of a SiPM. To prevent optical and electrical interference, each microcell is separated by a 'dead region'. The fill factor of a SiPM refers to the ratio of the active cell area over the total area.

An equivalent circuit of a SiPM is given in Fig. 2.6. The circuit is similar to the SPAD case but with the addition of a passive element that contains the unfired parallel microcells and a parasitic component due to the grid. [3] Using standard circuit rules, it is easy to show that having N microcells in parallel results in resistors and capacitors taking values of R/N and $N \cdot C$ respectively. Fig. 2.6 also takes

into account the number of microcells that are fired, N_f . Thus, the number of microcells that contribute to the passive component is given by $N - N_f$.

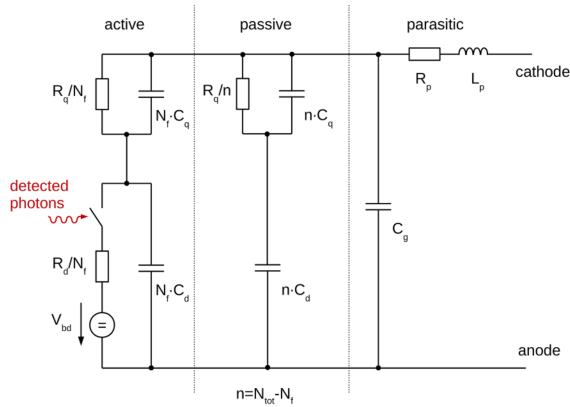


Fig. 2.6: Taken from [3]. An equivalent circuit of a SiPM.

The individual parameters in a SiPM, which need to be known for the model simulation, can be extracted experimentally. The quenching resistor, R_q , and the breakdown voltage, V_{br} , can be determined from the forward and backward IV (current-voltage) characteristics. Several methods in measuring V_{br} using the IV curve are compared in [13]. From Eq. 2.3, we can determine $C_d + C_q$ by measuring the gain. Finally, a CV plotter can be used to measure the conductance, Y_m , and the capacitance, C_m , at the SiPM terminals. It is then possible to write Y_m and C_m in terms of the parameters and therefore, when the value of $C_d + C_q$ is known, we are able to determine C_d , C_q and C_p . [14] The one remaining parameter is R_d . For this case, R_d can be assumed to have a value around $\sim 1k\Omega$. Simulations show that changing this value around this range does not affect the output greatly. [11]

In the following sections, we briefly review

some important properties of SiPMs. These are important to know in order to consider the feasibility of using such devices in the spark chamber trigger system.

2.3.2 Gain

Since the microcells are independent, the gain of a SiPM is proportional to the number of fired microcells. Using Eq 2.3:

$$G = \sum_i G_i = \sum_i \frac{(C_d + C_q)V_{ov}}{e} \quad (2.4)$$

This is only true if the microcells are connected in parallel without any additional impedances. In the SiPM equivalent model, we also have to consider the parasitic capacitances. In addition, the output signal is not proportional to the number of fired microcells if the preamplifier input impedance is not zero. [15] Hence, the gain is no longer linear with respect to the number of fired microcells.

It is worth, at this point, considering the effect of temperature on the gain. It is important to note that the gain is independent of temperature as long as the overvoltage ($V_{bias} - V_{br}$) remains fixed. However, the breakdown voltage, V_{br} , does depend on temperature since the mean free path of the charge carriers decreases with increasing temperature. Thus, a higher electric field is required to start the avalanche process effectively increasing V_{br} and lowering the overvoltage for a fixed bias voltage. [3] If the bias voltage is not changed to keep the overvoltage fixed, the gain decreases with increasing temperature.

2.3.3 Photon Detection Efficiency

The photon detection efficiency (PDE) is the probability that a photon arriving on the detector surface is detected. It is given by:

$$PDE = QE(\lambda) \times \epsilon \times P_T(V_{ov}, \lambda) \quad (2.5)$$

where QE is the quantum efficiency, ϵ is the fill factor and P_T is the probability of successfully triggering an avalanche. P_T depends on the overvoltage since the triggering probability depends on the electric field; a higher overvoltage increases P_T . The wavelength dependence is due to different absorption depths in the silicon for different wavelengths. The fill factor, ϵ , is the ratio of the active microcell region to the total SiPM area. [11]

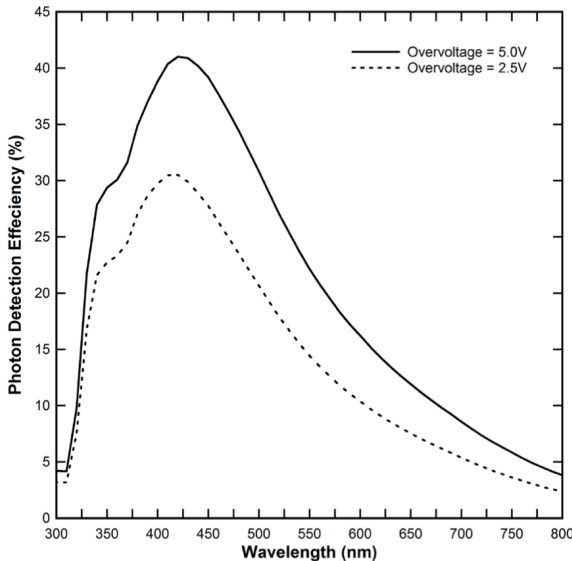


Fig. 2.7: Taken from [8]. How the PDE is affected by the photon wavelength. A higher overvoltage also increases the PDE since the microcell triggering probability is increased.

By definition, $0 < QE, \epsilon, P_T < 1$, so the PDE is maximised when all 3 factors are optimised.

QE values as high as 0.98 have been achieved. [16] Recent advances since 2010 have led to many SiPMs having comparable PDE values up to 60%. [3] Fig. 2.7 is an example of how the PDE varies with wavelength.

2.3.4 Primary Noise

Due to the high bias voltage, it is possible for microcells to be randomly triggered by thermally generated carriers. These dark counts follow a Poisson distribution and forms the primary noise for a SiPM. [7] It follows that reducing the bias voltage reduces the dark count rate (DCR).

The thermal generation of carriers and hence, the DCR obviously depends on the temperature and Fig. 2.8 shows this dependence; at 20°C , the $\text{DCR} \sim 1 \times 10^5 \text{ cps mm}^2$ where cps is the counts per second. In general, the DCR halves about every 10°C and at low temperatures, tunnelling effects dominate dependent on the internal electric field. As seen in Fig. 2.8, the DCR saturation at low temperatures is higher for a SiPM designed with a standard internal field structure than a low field one. [17]

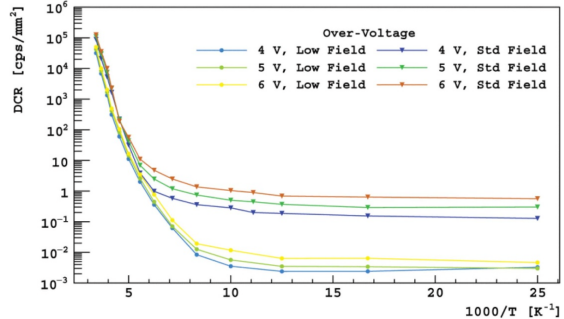


Fig. 2.8: Taken from [17]. The DCR decreases as the temperature decreases until it reaches a baseline value where tunnelling effects dominate.

It is interesting to note that there is evidence

so suggest that only a small percentage of microcells are responsible for most of the DCR: "some pixels have very high DCR compared to the median DCR value". [18]

2.3.5 Correlated Noise

Noise as a result of primary firing microcells is known as correlated noise (Fig. 2.9). There are two types of correlated noise: i) afterpulsing and ii) optical crosstalk. Afterpulsing is the result of trapped charged carriers during the initial microcell firing process. These trapped carriers are then released after the initial signal to create subsequent signals that are lower in amplitude since the microcell has not fully recovered. Afterpulsing can also be optically induced: each charge carrier in an avalanche produces approximately 3×10^5 secondary photons. [19] These secondary photons can be absorbed by the same microcell triggering another avalanche. Afterpulses increase an individual microcell's overall recovery time.

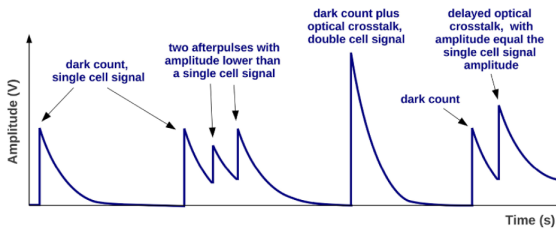


Fig. 2.9: Taken from [11]. Examples of correlated noise.

Optical crosstalk relates to the firing of neighbouring microcells due to the primary firing microcell. Similar to optically induced afterpulsing, the secondary photons can induce avalanches in neighbouring microcells. Considering just one adjacent microcell, the

crosstalk can be near instantaneous resulting in a signal with twice the amplitude (prompt crosstalk) or it can be delayed (delayed crosstalk). Delayed crosstalk events can generally be separated from the primary event due to the longer timescale. We see a secondary signal whose magnitude is the sum of the recovering primary microcell and the fired secondary microcell. Optical crosstalk can be reduced by adding trenches inbetween microcells; trenches increase the 'dead region' of the SiPM and hence, affects the fill factor of the overall cell. [3]

A simple model to describe the optical crosstalk probability is that, for N avalanches produced simultaneously via optical crosstalk, $P(N) \propto e^{-N}$. [11] Defining the crosstalk probability as the number of multi-photon events over the number of single photon events, a naive calculation gives a theoretical upper bound for the optical crosstalk probability:

$$P(\text{Crosstalk}) = e^{-1}(1 + e^{-1} + e^{-2} + \dots)$$

$$\rightarrow \frac{e^{-1}}{1 - e^{-1}} \approx 58.2\%$$

3 SPICE SIMULATIONS

3.1 Overview

LTspice [20] is a simulation software designed to simulate analog electronic circuits. By utilising an equivalent circuit model for a SiPM, it is possible to simulate the features and behaviours of such devices. These results can then be compared to real-world experimental data. The majority of simulations performed were transient analyses, allowing the response of the circuit to be measured based on the arrival of an incident signal.

The resulting output of a LTspice simulation can be exported as a tabulated ASCII file; an example is given in appendix B. These files were then processed using Python and the data graphed using Matplotlib. Some example code is presented in appendix C.

3.2 Unit Tests

A initial series of unit tests were performed to ensure: i) familiarity with the different features of the simulation software and ii) it was working as intended and producing sensible results.

3.2.1 Resistor Circuit

A DC sweep was performed on a simple resistor circuit (Fig. 3.1) with different resistance values and the resulting IV graph is shown in Fig. 3.2. As expected, we get a linear relationship from Ohm's law.

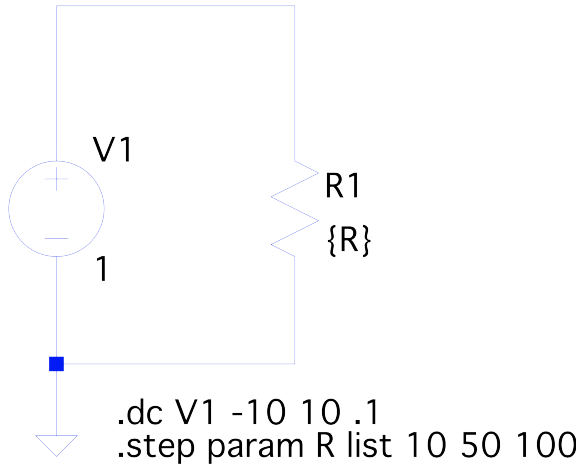


Fig. 3.1: A simple resistor circuit used in our unit test. The resistor takes values of 10Ω , 50Ω and 100Ω while the voltage source sweeps through DC values between $-10V$ and $10V$. The current through the resistor can be measured resulting in the expected IV graph.

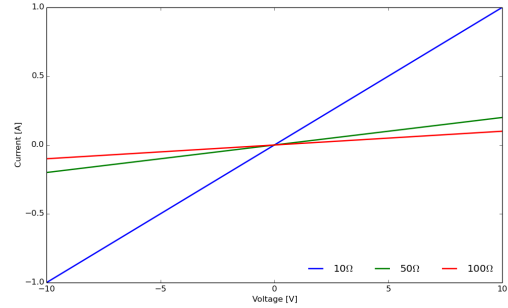


Fig. 3.2: The resulting IV graph for the resistor circuit.

3.2.2 RC Circuit

Two tests were performed on the RC circuit (Fig. 3.3). Firstly, a transient analysis simulates the circuit in the time domain. Using the values in Fig. 3.3, we can see that the charge and current of the capacitor over time is consistent with theory (Fig. 3.4).

Secondly, an AC analysis simulates the response of the circuit in the frequency domain ($V = e^{-i\omega t}$). The resulting Bode plot (Fig. 3.5) shows the frequency dependence of the RC circuit. As expected, the RC circuit acts as a potential divider dependent on frequency. This can also be shown to be consistent with theory analytically using standard circuit rules:

$$Z = R - \frac{i}{\omega C}$$

$$\left| \frac{V_R}{V_{in}} \right| = \frac{\omega RC}{\sqrt{1 + (\omega RC)^2}}, \phi_R = \frac{\pi}{2} - \tan^{-1}(\omega RC)$$

$$\left| \frac{V_C}{V_{in}} \right| = \frac{1}{\sqrt{1 + (\omega RC)^2}}, \phi_C = -\tan^{-1}(\omega RC)$$

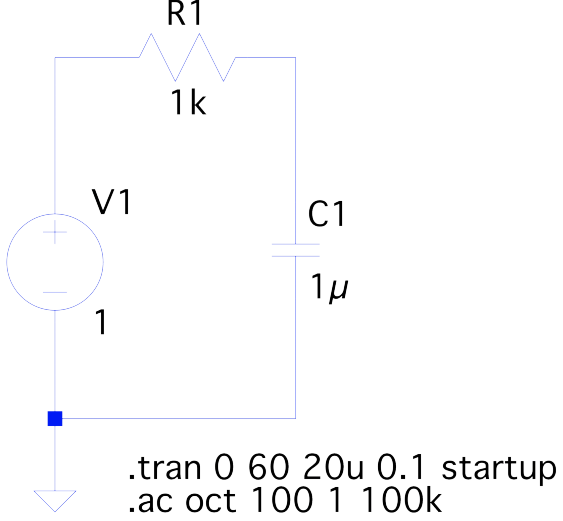


Fig. 3.3: A standard RC circuit with $R = 1k\Omega$ and $C = 1\mu F$. A transient analysis with a DC voltage of 1V simulates the charging of the capacitor (Fig. 3.4). An AC analysis with $V = e^{-i\omega t}$ generates a Bode plot between 1Hz and 100kHz. (Fig. 3.5)

3.3 SPAD Simulation

The equivalent circuit model for a SPAD used in our simulations is given in Fig 3.6. With the same approach as [11], we use a switch to simulate the arrival of a photon that triggers the circuit. For our purposes, we model the photon with a voltage signal that activates 10ns into the simulation and has a rise/fall time of 0.1ns. Since these simulations typically run in the region of tens of nanoseconds, we can effectively treat this signal as a delta function. Thus, the voltage signal models a photon impinging on the SPAD which closes the switch and triggers the circuit. An alternative method would be to use a direct current source. [14]

For convenience, we set the overvoltage to be 1V and the other parameters to be typical but idealised values. More realistic values are

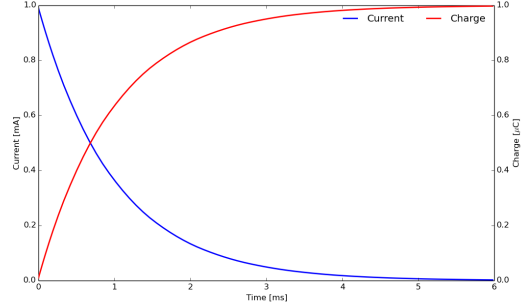


Fig. 3.4: A transient analysis of a RC circuit to simulate capacitor charging. With $R = 1k\Omega$ and $C = 1\mu F$, we have $\tau = 1ms$. We get the expected exponential relationships ($V = 1V$): $I = \frac{1}{R}e^{-t/\tau} \rightarrow 0A$ and $Q = C(1 - e^{-t/\tau}) \rightarrow 1\mu C$.

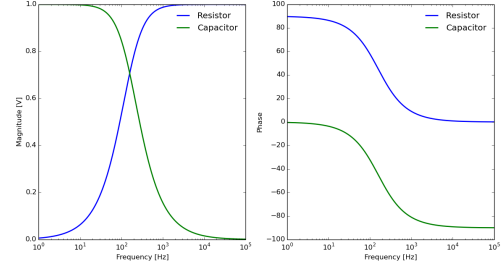


Fig. 3.5: An AC analysis of a RC circuit. Using standard circuit rules, we can see the results are in agreement with theory. For example, $\phi_C = -\tan^{-1}(\omega RC) \rightarrow -\frac{\pi}{2}$.

used when simulating the behaviour of a complete SiPM circuit. There are two main ways we can consider the behaviour of our system: by considering either the current through R_q or the voltage across C_d . It was found to be more convenient to measure the current for the most part especially when calculating the recovery time of the SPAD.

Three main sets of simulations were run for the SPAD. Firstly, various parameters in the circuit were varied including R_q , R_d and V_{ov} to determine the effect of each component on the resultant signal. Secondly, the effect

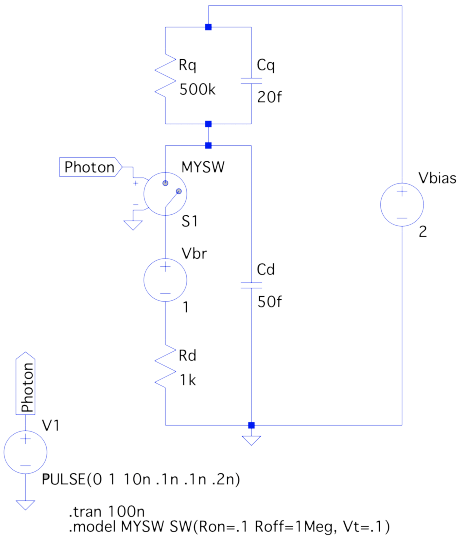


Fig. 3.6: The equivalent SPAD circuit used in the simulations. For convenience, the overvoltage was set to 1V. The arrival of a photon is simulated by a delta function voltage peak. This voltage peak briefly closes the switch causing the circuit to trigger.

of various parameters on the SPAD recovery time was studied and compared with theory (Eq. 2.2). Taking the logarithm of the current signal allowed the recovery time to be extracted via a linear regression. Finally, the theoretical value for the gain of a SPAD (Eq. 2.3) was tested by integrating the current to find the total charge. The most significant results are presented in Section 4.1.

3.4 SiPM Simulation

Fig. 3.7 shows the complete SiPM model used in our simulations and is an adaptation to the model used in [11]. The output signal of the SiPM is fed into a front-end amplifier based on our current existing experimental setup Fig. 3.8. There are two stages for the amplification process; both of which utilise the ADA4817 amplifier [21] to amplify and shape

the signal. Note that in the literature, the most common amplifier used in the amplification stage is the AD8000. [11][15] However, for most of our simulations, the amplifier was neglected in favour of taking the final signal directly from the SiPM output.

Model Parameter	SiPM ITC-irst	SiPM Photonique
V_{bias}	35V	63V
V_{br}	31.2V	61V
R_q	393k Ω	774k Ω
C_d	34.6fF	40.8fF
C_q	12.2fF	21.2fF
C_p	27.8pF	18.1pF

Table 1: Adapted from [14]. The known parameters of two different SiPMs used in our SiPM simulations.

In an identical fashion to the SPAD, the model uses a switch to simulate the triggering of the SiPM by a photon. For the model parameters, given that the parameters of our internal laboratory SiPM have not yet been determined, it was decided that values based on 2 known SiPMs should be used. These values are presented in Table 1. Two modifications have been made to this: i) the introduction of a shunt resistor, R_s and ii) allowing the total number of cells in the SiPM to vary. As a result, the parasitic capacitance of the circuit is now given by $C_p = NC_g + 15pF$ where $C_g = 0.02pF$ - reflecting a greater parasitic capacitance for a larger total number of microcells. In the case of R_d , the value was kept at 1k Ω since, as previously mentioned, changing R_d in the range of $\sim 1k\Omega$ doesn't affect the output too much. For our purposes, the SiPM was simulated with $N = 400$ and $N = 3600$ cells, corresponding to SiPMs of sizes $1 \times 1mm^2$ and $3 \times 3mm^2$ with a $50\mu m$ pitch respectively.

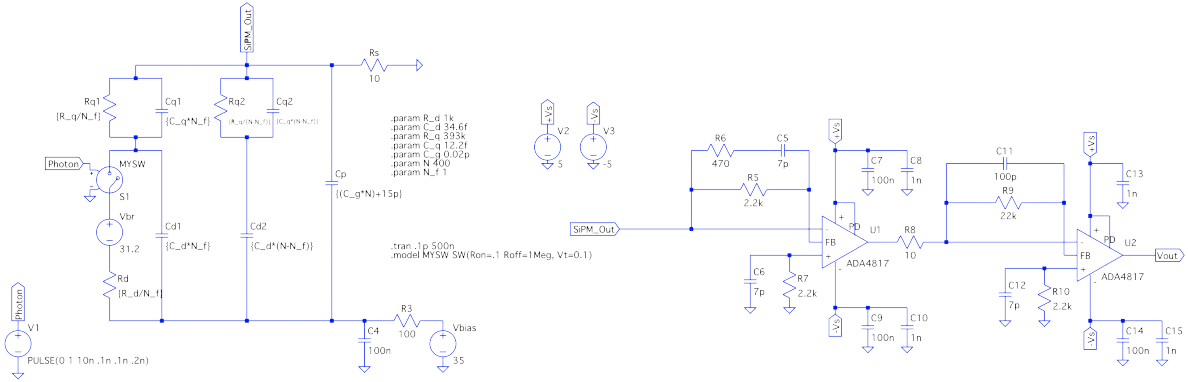


Fig. 3.7: The complete circuit model used in the simulations. The output of the SiPM is connected to an amplifier circuit based on Fig. 3.8. For most of our simulations, the amplifier was neglected and the voltage signal taken directly from the SiPM output.

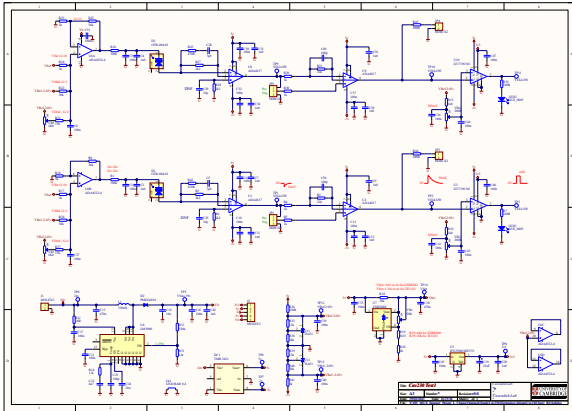


Fig. 3.8: The schematic for the amplifier circuitry that is connected to the SiPMs at the Cavendish Laboratory.

Similar to the SPAD, a number of different simulations were run. Firstly, the parameters were varied to determine their effects on the voltage signal at the SiPM output. In contrast to the SPAD, there are additional parameters to consider such as the total number of cells (N), the total number of fired cells (N_f) and the parasitic capacitance (C_p). Secondly, the effect of the parameters on the SiPM gain was investigated by taking the in-

tegral of the current through R_s . We shall see that the gain is now no longer linear due to the additional impedances.

Finally, we use an alternative method to calculate the SiPM microcell recovery time compared to the SPAD case. The subsequent triggering of the circuit simulating the arrival of a photon after the initial one leads to a second output signal. However, if the cell has not fully recovered, the second voltage peak is less than the initial one. We measure the minimum time it takes for the secondary photon to correspond to an output signal that is equal to the initial voltage peak. We also note the time for the secondary signal to be half the size as the initial one.

4 RESULTS AND DISCUSSION

4.1 SPAD Simulations

Simulating the SPAD circuit in Fig. 3.6, Fig. 4.1 recreates the resultant current signal

through R_q seen in Fig. 2.4 alongside the corresponding charge of the capacitor, C_d . We see that the behaviour of the current is reflected by the behaviour of the capacitor i.e. the current is exponentially decreasing while the capacitor is recharging.

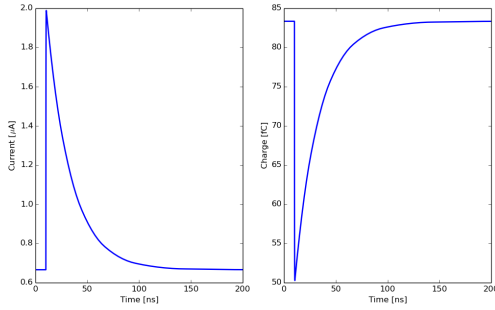


Fig. 4.1: A single SPAD simulation measuring the current through R_q and the charge of the capacitor, C_d .

4.1.1 Variation of Parameters

Fig. 4.2 shows the effect of varying R_q and R_d in the SPAD circuit. Increasing the quenching resistance has a noticeable effect on both the magnitude of the current and the recovery time. Note that, since we have set the overvoltage to 1V, decreasing the resistance much further will cause the current to exceed the operating limit of $20\mu A$. As expected, the variation of R_d has a negligible effect on the shape of the signal for values $R_d \sim 1k\Omega$ although it is possible to see the effect of varying R_d on the rising edge upon closer inspection. This is most evident for $R_d = 5k\Omega$ where the rise time is noticeably longer than for the other values.

Similarly, the effect of varying C_d is shown in Fig. 4.3. Again, as expected from Eq. 2.2, the recovery time increases as the capac-

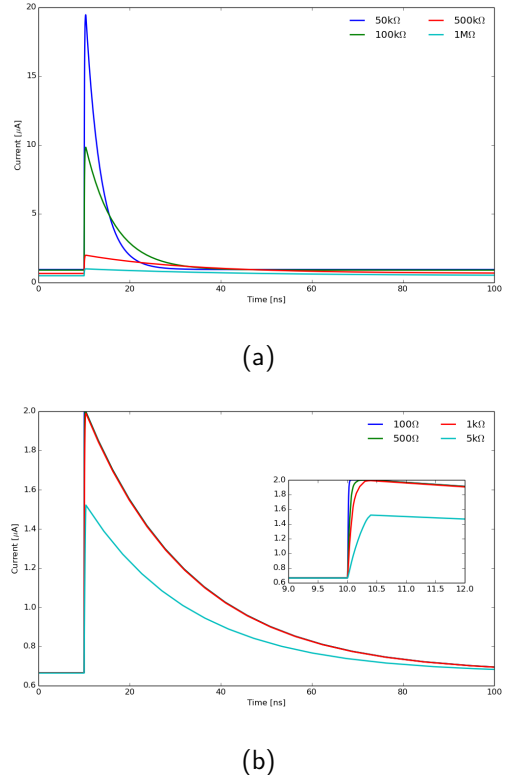


Fig. 4.2: The variation of a) R_q and b) R_d in the SPAD.

itance increases. A capacitor with a higher capacitance also discharges a larger amount of charge that contributes to the gain. This is imitated in the current graph by a larger integral value for higher capacitances.

Finally, we can see from Fig. 4.4 that no current is produced when the overvoltage is zero. Hence, there is no gain unless the biased voltage is about the breakdown voltage. As the overvoltage increases, we get an increased DC offset and gain.

4.1.2 Gain

The gain was computed by direct numerical integration of the current through the quench-

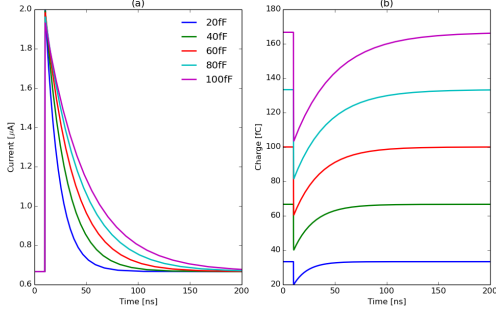


Fig. 4.3: The variation of C_d in the SPAD. The larger charge discharged by the capacitor at higher C_q corresponds to a higher gain.

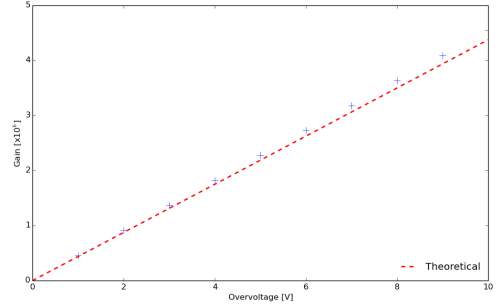


Fig. 4.5: Plot of the simulated gain value against the overvoltage. We see that it is consistent with theory: $G = \frac{(C_d + C_q)V_{ov}}{e}$.

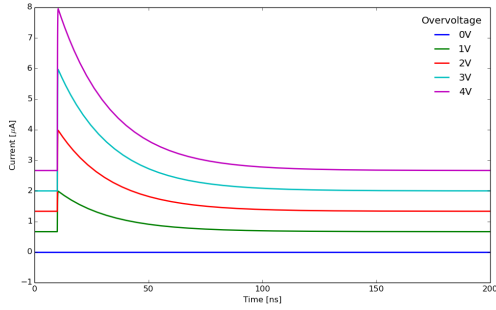


Fig. 4.4: The effect of the overvoltage on the signal; no current is produced when the overvoltage is zero.

ing resistor R_q with respect to time. The total charge was then divided by the elementary charge, q , to find the gain. Plotting the gain with respect to the overvoltage (Fig. 4.5) shows that the model is consistent with the theory (Eq. 2.3). It was found that Python's numerical integration using the trapezoidal rule and Simpson's rule produced similar results and so, for simplicity, the trapezoidal method was used. Note that when computing the integral, care must be taken to not include the current prior to the circuit triggering.

4.1.3 Recovery Time

The recovery time of the cell was extracted by taking the logarithm of the current signal falling edge and performing a linear regression; the recovery time is then the negative reciprocal of the gradient. Since $\tau_r = R_q(C_d + C_q)$ (Eq. 2.2), Fig. 4.6 compares the variation of these parameters with the theoretical value. We see that the model is consistent with the theory; the discrepancy between the calculated values and the theoretical value can be attributed to the way Spice outputs the discretised data. In addition, the simulated current signals do not exhibit ideal exponential decay and thus, the gradient is not perfectly linear.

4.2 SiPM Simulations

As previously mentioned, the parameter values for the SiPM simulations were based on measured values of other SiPMs (Table 1). The main difference being the parasitic capacitance of the circuit taking a simple form that is linear with the total microcell number: $C_p = NC_g + 15pF$ where $C_g = 0.02pF$. Fig. 4.7 shows the voltage taken at the output ter-

minal of the SiPM (neglecting the amplifier circuit) for the two different sets of parameter values with $N = 400$ and $N = 3600$. The signals corresponding to $N = 3600$ are smaller in magnitude and longer in recovery time reflecting the additional impedance from the parasitic component.

For convenience, we shall refer to the ‘FBK-Irst’ and ‘Photonique’ SiPMs as ‘SiPM 1’ and ‘SiPM 2’ respectively from now on. In addition, we shall focus our discussion on SiPM 1 since there are no additional insights that are gained from considering both. The equivalent, most significant results for SiPM 2 are presented in appendix D.

4.2.1 Variation of Parameters

Fig. 4.8(a) further shows the effect of varying the total number of microcells; note that the $N = 1$ case is equivalent to the SPAD presented earlier. The effect of increasing the number of fired microcells is shown in Fig. 4.8(b). We can clearly see that the amplitude of the output signal is proportional to the number of firing microcells. However, by simulating the saturation of the SiPM (Fig 4.9), the relationship is not directly linear. For a shunt resistance of 10Ω , doubling the number of fired microcells roughly increases the relative output voltage peak by 1.16.

Figs. 4.10-11 show the variation of the various resistors and capacitors in the SiPM circuit. We see, with the lowest quenching resistance, that the signal starts to resolve into a fast and a slow decay component. If the resistance is decreased further, we would see the voltage remain at a high value and no quenching occurs. The shunt resistor, R_s , offers a convenient way to practically probe the current at the SiPM terminal. In this case, in-

creasing the shunt resistance has the opposite effect to increasing the quenching resistance - the signal becomes less quenching with increasing shunt resistance.

Increasing the capacitance of C_d decreases the peak voltage signal whereas the opposite is true for C_q . However, the gain increases when we increase either C_d or C_q . Despite a lower signal peak when C_d is increased, there is a longer decay time down to the baseline value. The opposite is true for C_q where a higher signal peak also corresponds to a faster decay back down to baseline. In either case, the integral to find the gain is larger than the corresponding lower values. Unsurprisingly, increasing the parasitic capacitance lowers the voltage peak but increases the slow decay component.

4.2.2 Gain

The saturation up to 400 microcells to calculate the relative gain is shown in Fig. 4.12 and the results of a linear regression is presented in Table 2. Similar to the relative peak voltage, the nonlinearity is expected due to the additional impedances in the circuit. Interestingly, most of the values of the shunt resistance for SiPM 2 resulted in a relative gain per microcell greater than 1; this reflects the relative arbitrariness of how long the transient analysis should be ran for.

As expected, the gain is directly proportional to the overvoltage (Fig. 4.13) - a linear fit of $G = (3.73 \times 10^5 V^{-1})V_{ov}$ is obtained. A quadratic fit was found to be necessary for the dependency of C_d on the gain (Fig. 4.14(a)) while a linear fit was sufficient for C_q (Fig. 4.14(b)). The results obtained were:

Shunt Resistance [Ω]	SiPM 1	SiPM 2
1	0.854	1.12
10	0.837	1.08
50	0.795	1.03
100	0.753	0.983

Table 2: The linear regression values obtained from a plot of the relative gain against the number of firing microcells (see Fig. 4.12).

$$G = -(917fF^{-2})C_d^2 + (2.40 \times 10^5 fF^{-1})C_d - (5.77 \times 10^6)$$

and

$$G = (2.01 \times 10^5 fF^{-1})C_q - (1.13 \times 10^6)$$

respectively when the capacitances are quoted in fF . Note that it is possible for the gain to become negative at lower capacitance values - these are the unphysical regions of the model. Finally, the parasitic capacitance does not affect the gain (Fig. 4.14(c)) as expected.

4.2.3 Recovery Time

The method for determining the SiPM microcell recovery time was previously discussed. Fig. 4.15(a) shows how the time interval of the second photon affects the secondary voltage peak. We note down the minimal times it takes for the secondary signal to be half (τ_{HP}) and equal (τ_{FP}) to the original peak. Fig. 4.15(b) plots the relative size of the secondary peak against the time interval between the initial and secondary photons. The recovery times are given in Table 3.

Recovery Time	SiPM 1 [ns]	SiPM 2 [ns]
τ_{HP}	8.12 ± 0.87	18.1 ± 1.25
τ_{FP}	56.1 ± 1.72	139 ± 22

Table 3: The calculated recovery times for the 2 SiPMs. Error ranges were obtained from measuring the maximum deviations when adjusting the sensitivity of the model calculations.

There is a slight decrease in the recovery time as the overvoltage increases (Fig. 4.16). However, this behaviour is not seen for SiPM 2 and the recovery time remains relatively constant with overvoltage. Thus, we attribute this behaviour to how the discretised data is being handled when calculating these values. The shorter recovery times associated with SiPM 1 leads to larger error bars. Fig. 4.17 show how the recovery time changes when R_q , C_d and C_q are varied. Table 4 summarises the results of performing a linear regression on the full peak recovery time.

Varied Parameter	Linear Fit
R_q	$(0.128\text{ns } \Omega^{-1})R_q + 38.9\text{ns}$
C_d	$(1.78\text{ns } fF^{-1})C_d + 30.3\text{ns}$
C_q	$(2.04\text{ns } fF^{-1})C_q + 75.9\text{ns}$

Table 4: A linear fit of the recovery time with respect to the varied parameter

4.2.4 Amplifier Readout

For completeness, the readout with the amplifier circuit connected to the SiPM output is shown in Fig. 4.18.

4.3 Practical Application

Here we relate our knowledge of SiPMs back to the spark chamber and consider the practicality of using these devices as part of the trigger system. At $T = 20^\circ\text{C}$, $\text{DCR} \sim 1 \times 10^5 \text{ cps mm}^{-2}$. For N microcells per mm^2 and assuming the microcells fire independently with equal probability, we can model the dark count of a cell using a Poisson distribution with parameter, λ :

$$\lambda = \frac{\text{DCR} \cdot \tau}{N}$$

where τ denotes the characteristic timescale of interest. In our case, $\tau \sim 100\text{ns}$ - the timescale associated with a microcell's recovery time. Thus, the probability of the cell firing at least once:

$$\begin{aligned} P(N > 0) &= 1 - P(N = 0) \\ &= 1 - e^{-\lambda} \\ &\sim 2.5 \times 10^{-5}, \quad (\lambda = 2.5 \times 10^{-5}) \end{aligned}$$

Hence, if a photon arrives at the microcell surface, the probability that the microcell has already fired as a dark count is negligible and therefore, the microcell is ready to detect an incident photon. This simple analysis does not factor in the probability of afterpulses or optical crosstalk but these factors become negligible when we factor in that the scintillators have light yields of several thousands of photons per MeV. [22] Even a SiPM signal that corresponds to several photons is usually enough to distinguish a signal from noise given a suitable voltage threshold.

Let us assume further that we have two independent sensors at the top and bottom of a spark chamber. If the chamber height is $\sim 1\text{m}$

and cosmic rays move close to the speed of light, $v \sim c$, it will take $\sim 3.3\text{ns}$ for a cosmic ray to pass through the two sensors. Given a more lenient timescale of 10ns and repeating the above calculation, we can deduce that if we see (nearly) coincident signals in the two sensors, it is almost guaranteed to be a cosmic ray and not due to the random firing of the microcells. Due to the fast leading edge when a photon is detected, the use of SiPMs are theoretically ideal for use in this situation in series with a coincidence logic circuit.

5 CONCLUSION

In this project, we have considered how SiPMs can potentially be used as part of a spark chamber trigger system in replacement of traditional PMTs. A model of the SiPM has been built using software that simulates electrical circuits. These simulations allow us to simulate the functionality of a SiPM, providing further insight on how SiPMs operate and how individual parameters affect its performance. These simulations have been shown to be consistent with theory.

However, a SiPM model relies heavily on knowing the parameters for a specific SiPM. Due to circumstances, we have not yet been able to determine the parameters of the specific SiPM we have in the laboratory. These parameters can be determined through the methods discussed in this report.

Thus, the next steps are clear. We would need to be able to test the SiPM experimentally to further assess its suitability in a trigger system. Features such as the DCR can then be measured quantitatively to see the SiPM's real-world performance. Having a working model can be complementary to such a task

since real-world results can be fed back into the model.

Finally, there are also a lot of potential further simulations that can be run using this model. For example, additional cells can be added in parallel to the existing model to simulate optical crosstalk. Then, there are methods to simulate the circuit such that the rate of optical crosstalk is in line with experimental measurements.

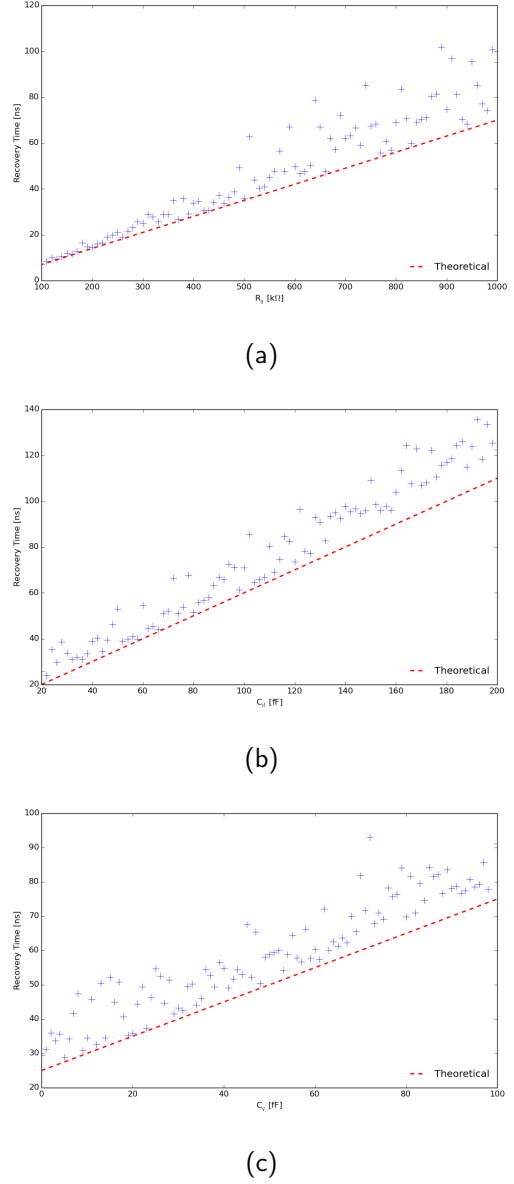


Fig. 4.6: The measured recovery time of the SPAD with respect to varying a) R_q , b) C_d and c) C_q .

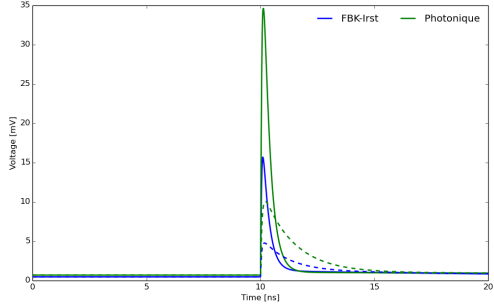


Fig. 4.7: The output voltage signal of the SiPM for the two sets of parameter values Table 1. Two values for the total number of microcells were simulated: $N = 400$ (solid line) and $N = 3600$ (dashed line).

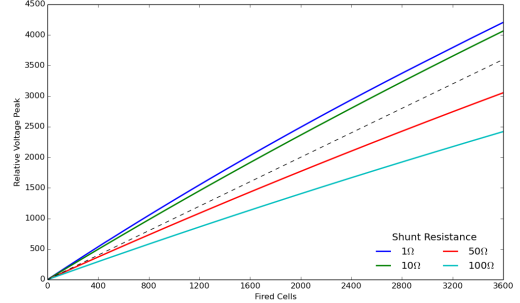
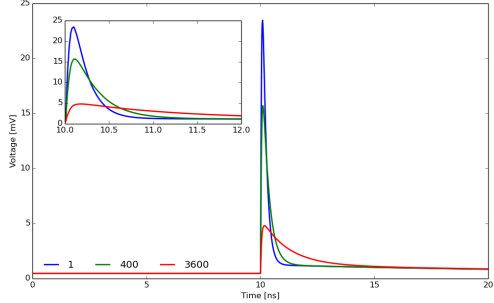
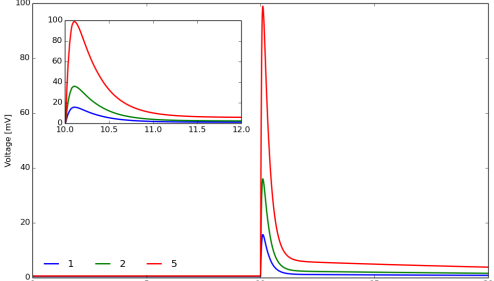


Fig. 4.9: For different shunt resistances, the relative peak voltage was calculated from a small number of fired microcells up to saturation at $N_f = 3600$. We get expected nonlinear behaviour due to the additional impedances in the SiPM.

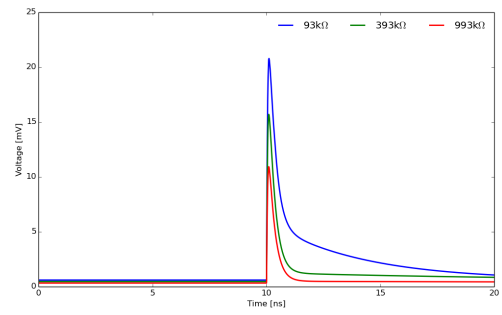


(a)

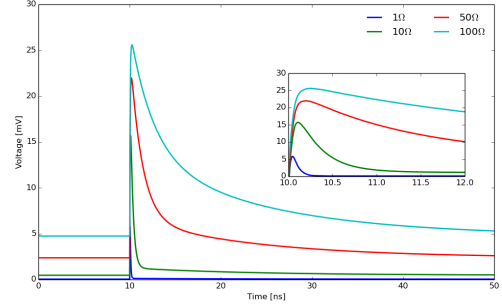


(b)

Fig. 4.8: Effect of a) varying the total number of microcells and b) the number of fired microcells on the output signal. Note that for (a), the $N = 1$ case reduces back down to the SPAD case. In (b), the voltage signal is proportional to the number of fired microcells.

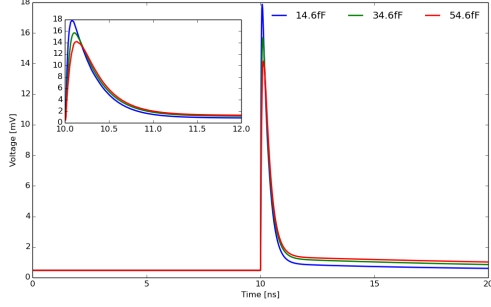


(a)

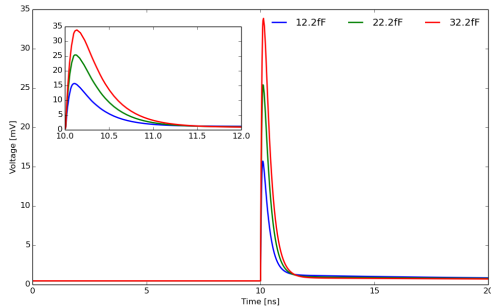


(b)

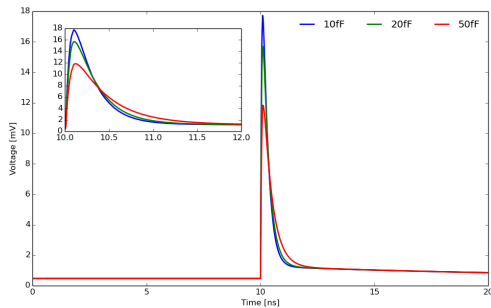
Fig. 4.10: Variation of a) R_q and b) the shunt resistance, R_s , in the SiPM. In (a) at $R = 93\text{k}\Omega$, we start to see the signal decay resolve into a fast and a slow decaying component.



(a)



(b)



(c)

Fig. 4.11: Variation of a) C_d , b) C_q and c) C_p in the SiPM.

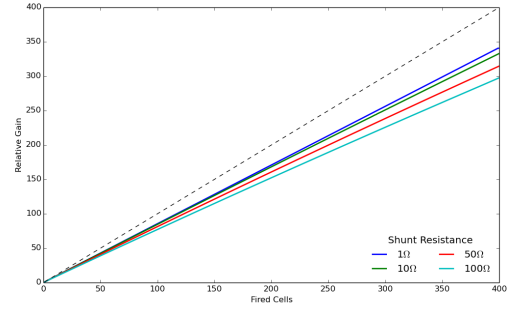


Fig. 4.12: For different shunt resistances, the relative gain compared to the single photon gain was calculated from a small number of fired microcells up to saturation at $N_f = 400$. The values obtained from a linear regression are given in Table 2.

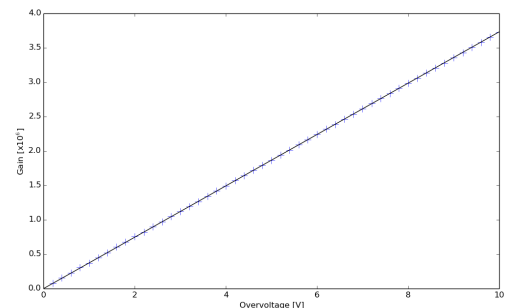
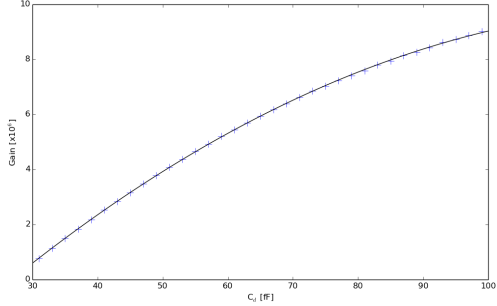
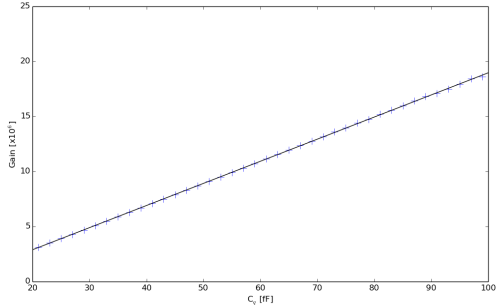


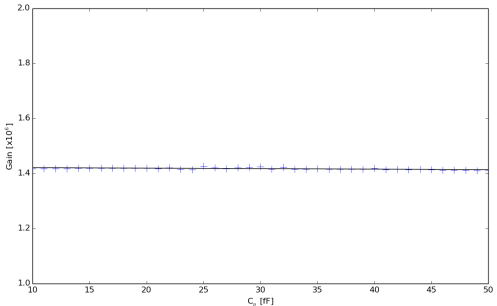
Fig. 4.13: Effect of the overvoltage on the SiPM gain. We get a linear fit: $G = (3.73 \times 10^5 V^{-1})V_{ov}$



(a)

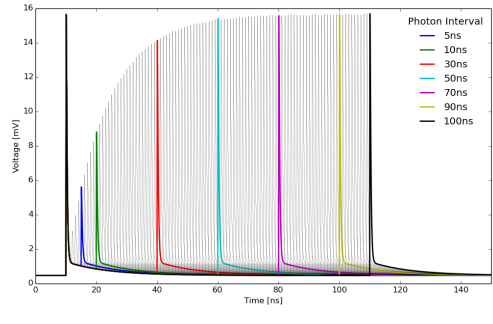


(b)

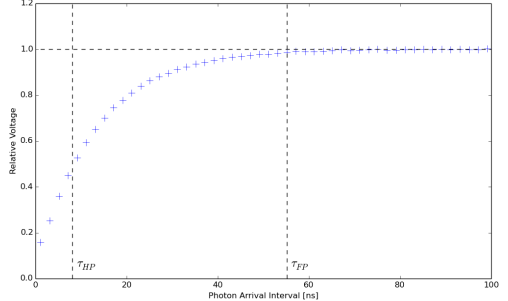


(c)

Fig. 4.14: Effect of varying a) C_d , b) C_q and c) C_p on the gain. A quadratic fit is required for (a). As expected, there is no effect of varying C_p on the gain since the parasitic component is independent and parallel to a firing microcell.



(a)



(b)

Fig. 4.15: To determine the SiPM microcell recovery time, a second photon triggers the circuit again after a specified time interval after the initial trigger. In (a), we see the secondary peak growing with an increasing time interval. The relative voltage peak of the secondary peak over time is shown in (b). The values of $\tau_{HP} = 8.12\text{ns}$ and $\tau_{FP} = 56.1\text{ns}$ are obtained.

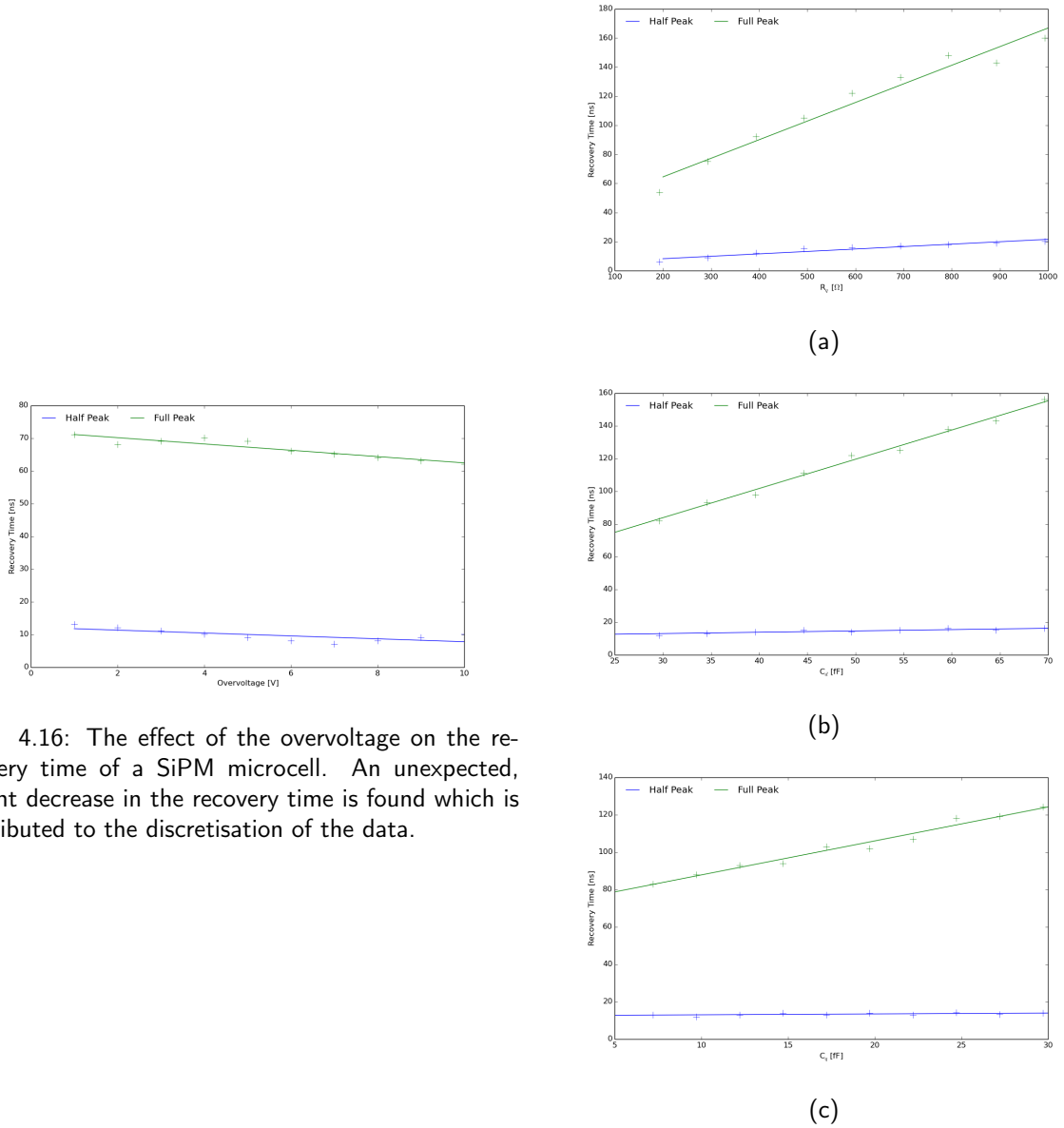


Fig. 4.16: The effect of the overvoltage on the recovery time of a SiPM microcell. An unexpected, slight decrease in the recovery time is found which is attributed to the discretisation of the data.

Fig. 4.17: Effect of varying a) R_q , b) C_d and c) C_q on the recovery time. The results of a linear fit on τ_{FP} are given in Table 4.

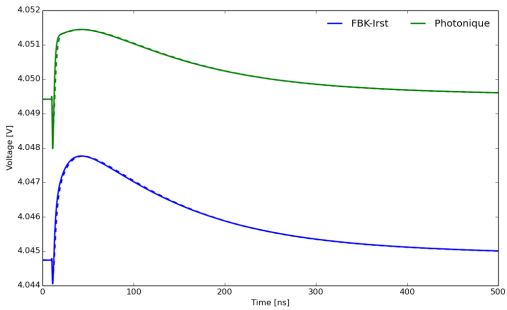


Fig. 4.18: Output at the end of the amplifier circuit when the 2 SiPM output signals are fed in. Again, two values for the total number of microcells were simulated: $N = 400$ (solid line) and $N = 3600$ (dashed line).

6 REFERENCES

- [1] Cambridge HEP Scatter! Website, *Spark Chamber*, Online at <https://www.hep.phy.cam.ac.uk/scatter/spark.html>, [Last accessed: 11th Apr 2021].
- [2] N. Dinu *et al.* [2007], *Development of the first prototypes of Silicon PhotoMultiplier (SiPM) at ITC-irst*, Nuclear Instruments and Methods in Physics Research Section A: Accelerators, Spectrometers, Detectors and Associated Equipment, Volume 572, Issue 1, Pages 422-426, ISSN 0168-9002, <https://doi.org/10.1016/j.nima.2006.10.305>.
- [3] S. Gundacker, A. Heering [2020], *The silicon photomultiplier: fundamentals and applications of a modern solid-state photon detector*, Phys. Med. Biol. **65** 17TR01, <https://doi.org/10.1088/1361-6560/ab7b2d>.
- [4] A. Vacheret *et al.* [2011], *Characterization and simulation of the response of Multi-Pixel Photon Counters to low light levels*, Nuclear Instruments and Methods in Physics Research Section A: Accelerators, Spectrometers, Detectors and Associated Equipment, Volume 656, Issue 1, Pages 69-83, ISSN 0168-9002, <https://doi.org/10.1016/j.nima.2011.07.022>.
- [5] S. Polyakov [2013], *Chapter 3 - Photomultiplier Tubes*, Experimental Methods in the Physical Sciences, Academic Press, Volume 45, Pages 69-82, ISSN 1079-4042, ISBN 9780123876959, <https://doi.org/10.1016/B978-0-12-387695-9.00003-2>.
- [6] R.J. McIntyre [1985] *Recent developments in silicon avalanche photodiodes*, Measurement, Volume 3, Issue 4, Pages 146-152, ISSN 0263-2241, [https://doi.org/10.1016/0263-2241\(85\)90024-7](https://doi.org/10.1016/0263-2241(85)90024-7).
- [7] S. Cova *et al.* [1996], *Avalanche photodiodes and quenching circuits for single-photon detection*, Appl. Opt. 35, 1956-1976.
- [8] SensL (Technical Note) [2011], *An Introduction to the Silicon Photomultiplier*, Online at <https://sensl.com/>, [Last accessed: 14th May 2021].
- [9] S. Gundacker *et al.* [2015] *On the comparison of analog and digital SiPM readout in terms of expected timing performance*, Nuclear Instruments and Methods in Physics Research Section A: Accelerators, Spectrometers, Detectors and Associated Equipment, Volume 787, Pages 6-11, ISSN 0168-9002, <https://doi.org/10.1016/j.nima.2014.10.020>.
- [10] S. Piatek [2014], *Measuring the electrical and optical properties of silicon photomultipliers*, Online at <https://hub.hamamatsu.com/jp/en/index.html>, [Last accessed: 14th Feb 2021].

- [11] F. Acerbi, S. Gundacker [2019], *Understanding and simulating SiPMs*, Nuclear Instruments and Methods in Physics Research Section A: Accelerators, Spectrometers, Detectors and Associated Equipment, Volume 926, Pages 16-35, ISSN 0168-9002, <https://doi.org/10.1016/j.nima.2018.11.118>.
- [12] D. Renker [2006], *Geiger-mode avalanche photodiodes, history, properties and problems*, Nuclear Instruments and Methods in Physics Research Section A: Accelerators, Spectrometers, Detectors and Associated Equipment, Volume 567, Issue 1, Pages 48-56, ISSN 0168-9002, <https://doi.org/10.1016/j.nima.2006.05.060>.
- [13] A. Nagai *et al.* [2019] *Characterization of a large area silicon photomultiplier*, Nuclear Instruments and Methods in Physics Research Section A: Accelerators, Spectrometers, Detectors and Associated Equipment, Volume 948, 162796, ISSN 0168-9002, <https://doi.org/10.1016/j.nima.2019.162796>.
- [14] F. Corsi *et al.* [2007], *Electrical Characterization of Silicon Photo-Multiplier Detectors for Optimal Front-End Design*, 2006 IEEE Nuclear Science Symposium Conference Record, Pages 1276-1280, <https://doi.org/10.1109/NSSMIC.2006.356076>.
- [15] S. Seifert *et al.* [2010], *Simulation of Silicon Photomultiplier Signals*, IEEE Transactions on Nuclear Science, 56 (6), 2009, <https://doi.org/10.1109/TNS.2009.2030728>.
- [16] First Sensor (White Paper) [2015], *Introduction to Silicon Photomultipliers (SiPMs)*, Online at <https://www.first-sensor.com/en/>, [Last accessed: 14th May 2021].
- [17] F. Acerbi *et al.* [2017], *Cryogenic Characterization of FBK HD Near-UV Sensitive SiPMs*, IEEE Transactions on Electron Devices, Vol. 64, No. 2, pp. 521-526, <https://doi.org/10.1109/TED.2016.2641586>.
- [18] S. Mandai, E. Charbon [2012], *Multi-channel digital SiPMs: Concept, analysis and implementation*, 2012 IEEE Nuclear Science Symposium and Medical Imaging Conference Record (NSS/MIC), pp. 1840-1844, <https://doi.org/10.1109/NSSMIC.2012.6551429>.
- [19] A. L. Lacaita *et al.* [1993], *On the bremsstrahlung origin of hot-carrier-induced photons in silicon devices*, IEEE Transactions on Electron Devices, Vol. 40, No. 3, pp. 577-582, <https://doi.org/10.1109/16.199363>.
- [20] Analog Devices, *LTspice Software*, Online at <https://www.analog.com/en/design-center/design-tools-and-calculators/ltpsice-simulator.html>, [Last accessed: 15th Apr 2021].
- [21] Analog Devices, *ADA4817-1 Amplifier*, Online at <https://www.analog.com/en/products/ada4817-1>, [Last accessed: 13th May 2021].

- [22] D. Herbert, *et al.* [2006], *First results of scintillator readout with silicon photomultiplier*, Nuclear Science, IEEE Transactions on. 53. 389 - 394, <https://doi.org/10.1109/TNS.2006.869848>.

APPENDICES

A EFFECT OF COVID-19

The COVID-19 pandemic has meant that Part III students were unable to carry out any experimental work at the Cavendish Laboratory. As a result, this project has been adapted to be one of a computational nature. Initially, the plan for this project was to be able to handle and perform experiments on the SiPMs directly in order to assess their suitability for operating in a spark chamber. However, due to the pandemic, we relied on the simulation of a SiPM using equivalent circuit models.

B SPICE OUTPUT FILE

```
time V(sipm_out)
Step Information: C_q=12.2f  (Run: 1/3)
0.0000000000000e+00 4.748553e-04
1.00000003627494e-15 4.748553e-04
2.00000007254987e-15 4.748553e-04
4.000000014509975e-15 4.748553e-04
8.000000029019950e-15 4.748553e-04
...
4.996054687500080e-08 5.146755e-04
5.0000000000000e-08 5.145579e-04
Step Information: C_q=22.2f  (Run: 2/3)
0.0000000000000e+00 4.748553e-04
1.00000003627494e-15 4.748553e-04
4.000000014509975e-15 4.748553e-04
...
Step Information: C_q=32.2f  (Run: 3/3)
0.0000000000000e+00 4.748553e-04
1.00000003627494e-15 4.748553e-04
2.000000007254987e-15 4.748553e-04
...
4.996054687500080e-08 5.244602e-04
5.0000000000000e-08 5.243570e-04
```

C EXAMPLE CODE

Some examples of code used in the project are presented here. An example of a SPICE output file is presented in appendix B and the subsequent code is used to treat such files. In general, the code parses the SPICE output file and separates the different variable values into its own subarray. We can then perform calculations on the arrays and plot any necessary graphs.

C.1 example1.py

```
1 # -----
2 # AUTHOR: [REDACTED]
3 # crsID: [REDACTED]
4 # COLLEGE: [REDACTED]
5 # DATE: Feb 2021
6 # PURPOSE: Part III Project - Creates a graph using matplotlib from a
7 #           LTSpice output data file (see appendix B).
8 # -----
9
10 import numpy as np
11 import matplotlib.pyplot as plt
12
13 counter = 0 # used to separate multiple data streams e.g. an IV graph with
#               different resistance values
14
15 # -----
16 # SPECIFY FILE HERE:
17 # -----
18
19 f = open("FILE_PATH", "r")
20
21 # -----
22 # Initialises global data arrays
23 # -----
24
25 # Ignore header lines
26 f.readline()
27 f.readline()
28
29 # iterates through every line in the Spice output file and determines the
#   number of data streams
30 for line in f:
31     line = line.strip()
32     row = line.split()
33     try: # test if the line contains data values
34         floatTest = float(row[1])
35     except ValueError:
```

```

36         counter += 1
37
38 # very generic variable names but avoids confusion when parsing different
# files with different variables e.g. resistance/capacitance data
39 xVar = [[] for i in range(counter+1)]
40 yVar = [[] for i in range(counter+1)]
41 graphLabel = np.array([[]])
42
43 # -----
44 # Helper functions
45 #
46
47 def appendArray(data , count):
48     global xVar, yVar
49     xVar[count] = np.append(xVar[count], float(data[0]))
50     yVar[count] = np.append(yVar[count], float(data[1]))
51     return
52
53 #
54 # Main function
55 #
56
57 # reset back to beginning of the file
58 counter = 0
59 f.seek(0)
60 f.readline()
61
62 # iterates through every line in the Spice output file again and adds every
# line of data into an array
63 for line in f:
64     # print(repr(line))
65     line = line.strip()
66     row = line.split()
67     # variable[0] = np.append(variable[0],1.1)
68     # print(variable)
69
70     try: # test if the line contains data values
71         floatTest = float(row[0])
72     except ValueError:
73         counter += 1
74         graphLabel = np.append(graphLabel, row[2])
75         continue # moves on to next line if the line does not contain data
76
77     appendArray(row , counter - 1)
78
79 f.close()
80
81 #
82 # Plot graphs

```

```

83 # -----
84
85 fig = plt.figure(figsize=(12, 7))
86 for i in range(len(xVar)):
87     label = graphLabel[i][4:-1] # extracts the parameter value
88     plt.plot(xVar[i]*1E9, yVar[i]*1E3, linewidth = 2, label = label)
89
90 plt.xlabel('Time [ns]')
91 plt.ylabel('Voltage [mV]')
92 plt.legend(frameon=False)
93
94 plt.savefig("FILE_PATH")
95 plt.show()

```

C.2 example2.py

```

1
2 # -----
3 # AUTHOR: [REDACTED]
4 # crsID: [REDACTED]
5 # COLLEGE: [REDACTED]
6 # DATE: Feb 2021
7 # PURPOSE: Part III Project – Parses through a specified number of files
    and performs a linear regression of the data in each file.
8 # -----
9
10 import numpy as np
11 import matplotlib.pyplot as plt
12 from scipy import optimize
13
14 counter = 0 # used to separate multiple data streams e.g. an IV graph with
    different resistance values
15 numFiles = 4 # number of files to loop over
16
17 # -----
18 # SPECIFY FILE HERE:
19 # -----
20
21 f = open("FILE_PATH", "r")
22
23 # -----
24 # Initialises global data arrays
25 # -----
26
27 # Ignore header lines
28 f.readline()
29 f.readline()
30
31 for line in f:

```

```

32     line = line.strip()
33     row = line.split()
34     try: # test if the line contains data values
35         floatTest = float(row[1])
36     except ValueError:
37         counter += 1
38
39     voltageRs1 = [[] for i in range(counter+1)] # Rs = 1
40     voltageRs2 = [[] for i in range(counter+1)] # Rs = 10
41     voltageRs3 = [[] for i in range(counter+1)] # Rs = 50
42     voltageRs4 = [[] for i in range(counter+1)] # Rs = 100
43
44 f.close()
45
46 #
47 # Helper functions
48 #
49
50 def appendArray(data, count, array):
51     array[count] = np.append(array[count], float(data[1]))
52     return
53
54 def linFunc(x, m):
55     return m*x
56
57 #
58 # Main function
59 #
60
61 # Loops over number of files
62 for i in range(1, numFiles + 1):
63     counter = 0
64     filePath = "FILE_PATH" + str(i) + ".txt" # opens text files named xxx1.
65     txt, xxx2.txt, ...
66     f = open(filePath, "r")
67
68     f.readline()
69
70     for line in f:
71         line = line.strip()
72         row = line.split()
73
74         try: # test if the line contains data values
75             floatTest = float(row[0])
76         except ValueError:
77             counter += 1
78             continue # moves on to next line if the line does not contain
79             data
80

```

```

79     if(i == 1):
80         appendArray(row, counter - 1, voltageRs1)
81     elif(i == 2):
82         appendArray(row, counter - 1, voltageRs2)
83     elif(i == 3):
84         appendArray(row, counter - 1, voltageRs3)
85     else:
86         appendArray(row, counter - 1, voltageRs4)
87
88 f.close()
89
90 # find the peak value of a single fired cell and calculates ratio: peak /
91 # single cell peak
92 firedCells = np.array(range(1, len(voltageRs1) + 1))
93 singleCellPeak1 = np.amax(voltageRs1[0])
94 singleCellPeak2 = np.amax(voltageRs2[0])
95 singleCellPeak3 = np.amax(voltageRs3[0])
96 singleCellPeak4 = np.amax(voltageRs4[0])
97
98 for i in range(len(voltageRs1)):
99     voltageRs1[i] = np.amax(voltageRs1[i]) / singleCellPeak1
100    voltageRs2[i] = np.amax(voltageRs2[i]) / singleCellPeak2
101    voltageRs3[i] = np.amax(voltageRs3[i]) / singleCellPeak3
102    voltageRs4[i] = np.amax(voltageRs4[i]) / singleCellPeak4
103 #
104 # Linear fit
105 #
106
107 params, covariance = optimize.curve_fit(linFunc, firedCells, voltageRs1)
108 params2, covariance2 = optimize.curve_fit(linFunc, firedCells, voltageRs2)
109 params3, covariance3 = optimize.curve_fit(linFunc, firedCells, voltageRs3)
110 params4, covariance4 = optimize.curve_fit(linFunc, firedCells, voltageRs4)
111
112 print(params, params2, params3, params4)

```

C.3 example3.py

```

1 #
2 #
3 # AUTHOR: [REDACTED]
4 # crsID: [REDACTED]
5 # COLLEGE: [REDACTED]
6 # DATE: Feb 2021
7 # PURPOSE: Part III Project – Calculates and plots the gain against
# overvoltage of the SiPM by via the integral of the current. A linear
# regression is performed on the data.
8 #
9

```

```

10 import numpy as np
11 import matplotlib.pyplot as plt
12 import scipy.integrate as integrate
13 from scipy import optimize
14
15 counter = 0 # used to separate multiple data streams e.g. an IV graph with
               different resistance values
16
17 # -----
18 # SPECIFY FILE HERE:
19 # -----
20
21 f = open("FILE_PATH", "r")
22
23 # -----
24 # Initialises global data arrays
25 # -----
26
27 # Ignore header lines
28 f.readline()
29 f.readline()
30
31 for line in f:
32     line = line.strip()
33     row = line.split()
34     try: # test if the line contains data values
35         floatTest = float(row[1])
36     except ValueError:
37         counter += 1
38
39 xVar = [[ ] for i in range(counter+1)]
40 yVar = [[ ] for i in range(counter+1)]
41 graphLabel = np.array([ ])
42
43 # -----
44 # Helper functions
45 # -----
46
47 def appendArray(data, count):
48     global xVar, yVar
49     xVar[count] = np.append(xVar[count], float(data[0]))
50     yVar[count] = np.append(yVar[count], float(data[1]))
51     return
52
53 def linFunc(x, m):
54     return m*x
55
56 # -----
57 # Main function

```

```

58 # -----
59
60 # Reset back to beginning of the file
61 counter = 0
62 f.seek(0)
63 f.readline()
64
65 for line in f:
66     # print(repr(line))
67     line = line.strip()
68     row = line.split()
69     # variable[0] = np.append(variable[0],1.1)
70     # print(variable)
71
72     try: # test if the line contains data values
73         floatTest = float(row[0])
74     except ValueError:
75         counter += 1
76         graphLabel = np.append(graphLabel, row[2])
77         continue # moves on to next line if the line does not contain data
78
79     appendArray(row, counter - 1)
80
81 f.close()
82
83 # -----
84 # Calculate gain
85 # -----
86
87 ELECTRON_CHARGE = 1.6E-19
88
89 # SiPM 1 parameters
90 V_BREAK = 31.2
91 C_d = 34.6E-15
92 C_q = 12.2E-15
93 C_p = 23E-15
94
95 gain = np.zeros(len(xVar))
96 overvoltage = np.zeros(len(xVar))
97 theoretical = np.zeros(len(xVar))
98
99 for i in range(len(xVar)):
100     gain[i] = np.trapz(yVar[i], xVar[i]) / ELECTRON_CHARGE
101     overvoltage[i] = float(graphLabel[i][6:]) - V_BREAK
102
103 gain = gain - gain[0]
104
105 # -----
106 # Linear fit

```

```

107 # -----
108
109 params, covariance = optimize.curve_fit(linFunc, overvoltage, gain)
110 # print params
111
112 # -----
113 # Plot graphs
114 # -----
115
116 fig = plt.figure(figsize=(12, 7))
117 plt.plot(overvoltage, gain*1E-6, '+', markersize=10)
118 plt.plot(overvoltage, linFunc(overvoltage, params[0])*1E-6, 'k') # linear
    fit of the data
119 plt.xlabel('Overvoltage [V]')
120 plt.ylabel('Gain [x10$^{6}]')
121 plt.legend(frameon=False)
122
123
124 plt.savefig("FILE_PATH")
125 plt.show()

```

D SiPM 2 RESULTS

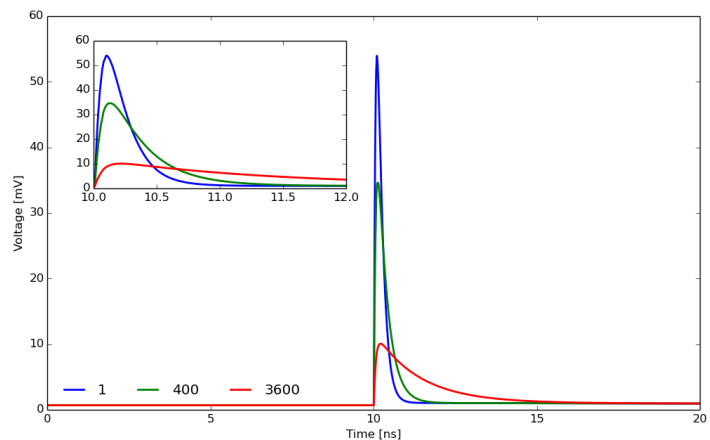


Fig. D.1: Variation of the total number of microcells and the resultant voltage signals.

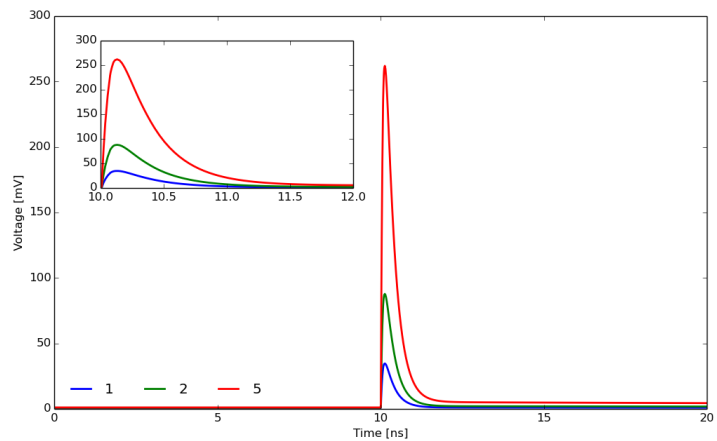


Fig. D.2: Variation of the number of fired microcells and the resultant voltage signals.

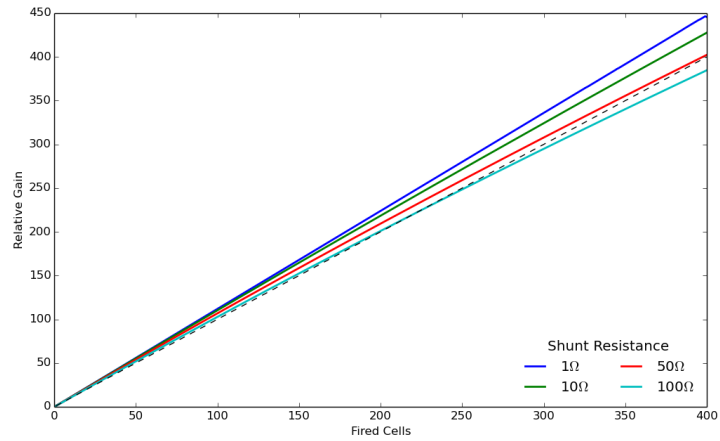


Fig. D.3: The relative gain from a single firing microcell up to the saturation of the SiPM ($N = 400$).

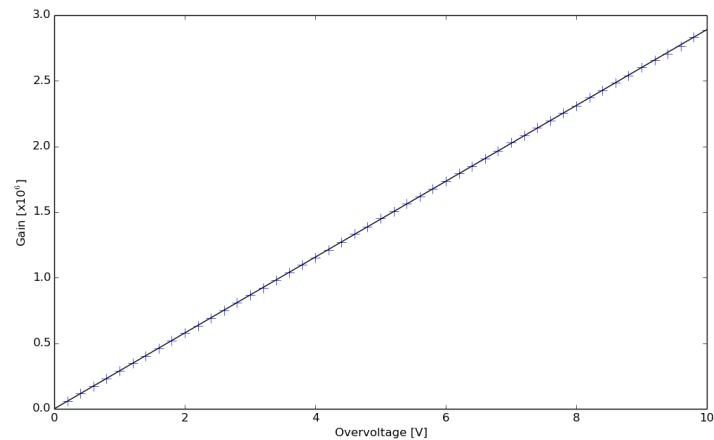


Fig. D.4: $G = (2.89 \times 10^5 V^{-1}) V_{ov}$

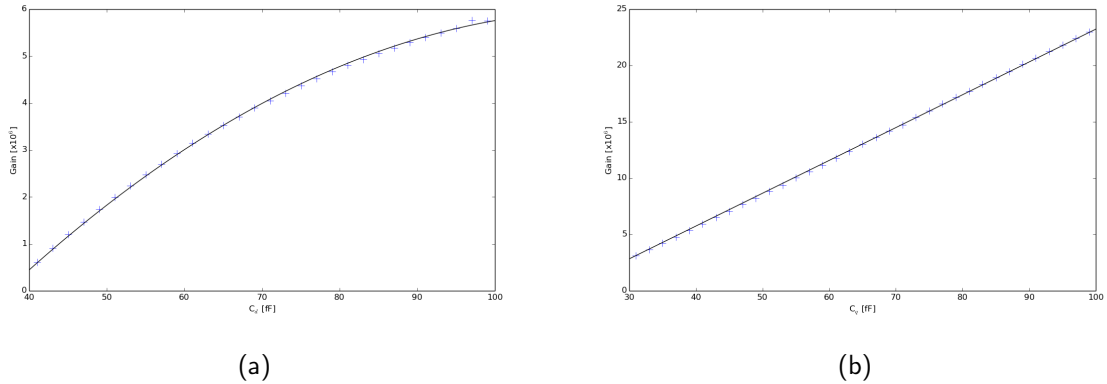


Fig. D.5: (a) $G = -(990fF^{-2})C_d^2 + (2.27 \times 10^5 fF^{-1})C_d - (7.06 \times 10^6)$ and (b) $G = (2.91 \times 10^5 fF^{-1})C_q - (5.90 \times 10^6)$

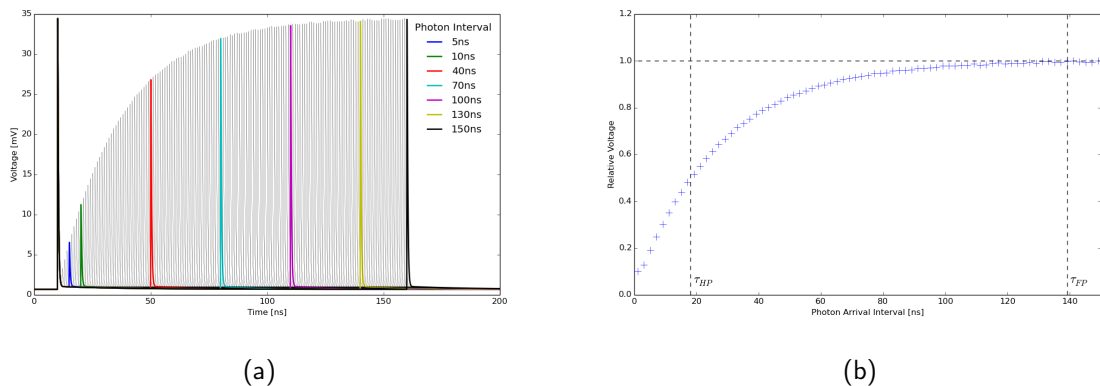
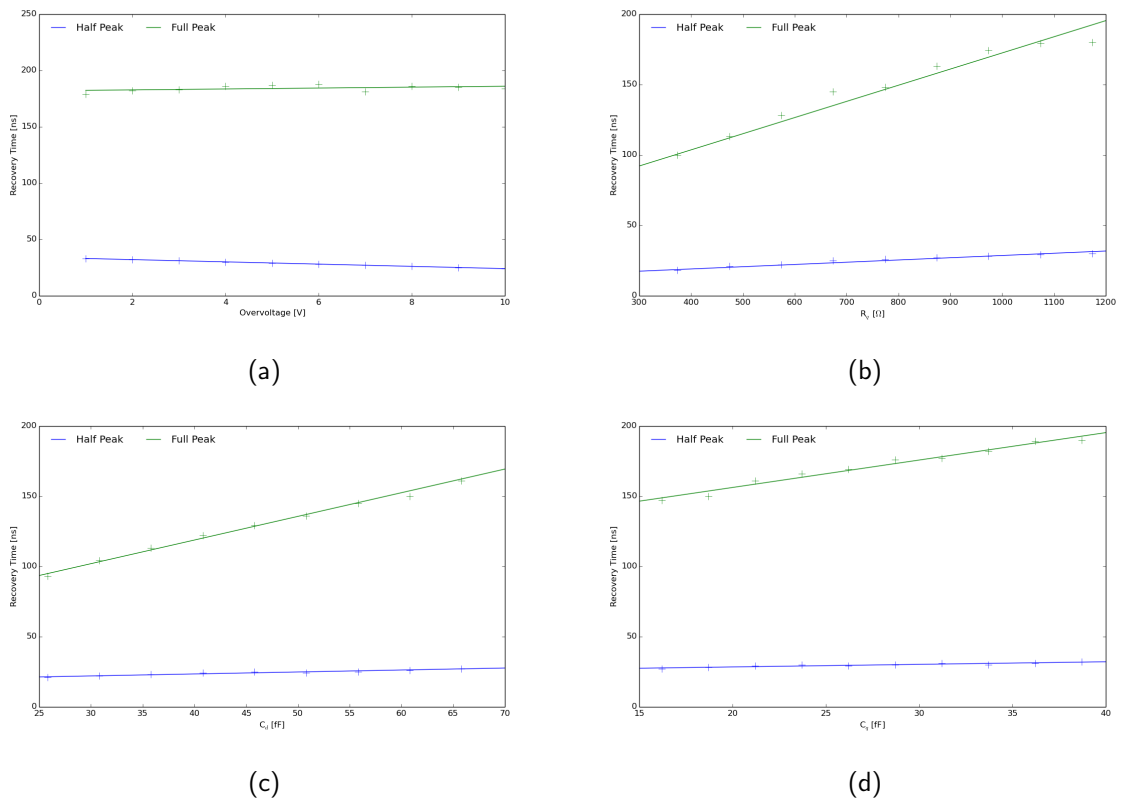


Fig. D.6: Recovery values of $\tau_{HP} = 18.1\text{ns}$ and $\tau_{FP} = 139\text{ns}$ are obtained.



D.7: Effect of varying (a) V_{ov} , (b) R_q , (c) C_d and (d) C_q on the recovery time.